ORIGINAL ARTICLE   **Open Access**

Closure Effect of I + II Mixed-mode Crack for EA4T Axle Steel

Shuancheng Wang[1], Bing Yang[1*] , Shuwei Zhou[1,2], Jian Li[1] and Shoune Xiao[1]

Abstract

The crack-closure effect is a crucial factor that affects the crack growth rate and should be considered in simulation analysis and testing. A mixed-mode I + II loading fatigue crack growth test was performed using EA4T axle steel specimens. The variation of the plastic-induced crack closure (PICC) effect and the roughness-induced crack closure (RICC) effect during crack deflection in the mixed-mode is examined in this study. The results show that the load perpendicular to the crack propagation direction hinders the slip effect caused by the load parallel to the crack propagation direction under mixed-mode loading, and the crack deflection is an intuitive manifestation of the interaction between the PICC and RICC. The proportion of the R_A value change on the crack side caused by contact friction was reduced by the interaction between PICC and RICC. The roughness of the crack surface before and after the crack deflection is different, and the spatial torsion crack surface is formed during the crack propagation process. With the increase of the crack length, the roughness of the fracture surface increases. During the crack deflection process, the PICC value fluctuates around 0.2, and the RICC value is increased to 0.15.

Keywords Crack closure, Crack deflection, Plasticity-induced closure, Roughness-induced closure, Interaction mechanism

1 Introduction

Fatigue damage and fracture are inevitable phenomena in the service life of engineering structures and materials [1]. When fatigue damage accumulates to a certain level, local plastic deformation occurs at the location of the highest stress region. Plastic deformation is one of the significant reasons for the occurrence of crack closure effects, and the existence of crack closure effects is conducive to restraining the opening of the crack. The crack closure effect encompasses factors such as plasticity, roughness, the presence of oxides, the small crack phenomenon, overload, and compression overload [2–4]. A reasonable understanding and application of the closure

effect contribute to researchers in engineering structure design and lifespan assessment.

Cracks can be divided into three types based on linear elastic fracture mechanics (LEFM): opening (type I), sliding (type II), and tearing types (type III), the different operating conditions in actual service lead to fatigue cracks in either isolated or mixed forms. To provide a reasonable description or assessment of the process of crack propagation, researchers have conducted long-term and systematic theoretical and experimental studies [5–9], including methods related to the Elber crack closure model, the incremental (or partial) crack closure model, and the zero crack propagation load method. With the help of relevant experimental methods, the relationship between the crack growth rate determined by far-field loading conditions, crack geometry and the stress intensity factor range (ΔK) under small-scale yield conditions is established. The contribution of oxidation or roughness to crack closure is shown to be smaller than the contribution of the slope change of the load-displacement

*Correspondence:
Bing Yang
yb@swjtu.edu.cn
[1] State Key Laboratory of Rail Transit Vehicle System, Southwest Jiaotong University, Chengdu 610031, China
[2] Institute of Metal Forming, RWTH Aachen University, 52064 Aachen, Germany

Wang *et al. Chinese Journal of Mechanical Engineering*   (2024) 37:81

Page 2 of 15

curve. In addition, the plastic strain-related mechanism at the crack tip can explain most of the test results, but some test results cannot be explained according to the plastic-induced crack closure (PICC) effect, and even contradict the crack closure method, other factors may play a role, such as the degradation of material mechanical properties (hardening and softening) during creep-fatigue process, and interaction between micro defects and microstructure (metal inclusions) [10, 11].

Research on the crack closure effect mainly focuses on PICC, roughness-induced crack closure (RICC) and oxide-induced crack closure (OICC) effects. Under the condition of uniaxial loading, materials are prone to PICC. Under mixed-mode loading conditions, crack deflection leads to mutual contact between fracture surfaces, resulting in the RICC effect. In humid environments, some materials are subject to OICC effects, as fatigue crack surfaces come into contact with the air, initiating oxidation-reduction reactions that accumulate oxidation-reduction products on the fracture surfaces. Peters and Yamaguchi et al. [12, 13] presented a non-contact full-field optical measurement method to investigate the PICC effects. McClung [14] used an elastic-plastic finite element method (FEM), which is considered PICC, to simulate fatigue crack propagation (FCG), the traditional Irwin-Rice estimate for crack tip plastic zone size in plane stress is found to be generally consistent with the FEM results. Christopher et al. [15, 16] established a new crack-tip stress field model (Christopher–James–Patterson, CJP model) based on the traditional Westergaard's model, the results show that the CJP model can better explain the PICC effect. Yang et al. [17] used the Levenberg-Marguardt (L-M) iterative method to solve for the crack tip position and apply it to the CJP crack tip field model. Li et al. [18] considered the effect of the dislocation field on the plastic zone of the crack tip and hence on the elastic field by introducing a plastic flow factor ρ, the plastic flow correction provides a more accurate crack tip field model and improves the CJP crack growth relationship. Yang et al. [19] applied the CJP model to the FCG of U71MnG rail steel standard compact tensile (CT) specimens, the results point out that the CJP model can describe the contour of the plastic zone, and can characterize the influence of crack tip compatible stress and the crack closure effect on crack propagation under different stress ratios. Paysan et al. [20] applied an elastic–plastic 3D FEM to study the evolution of plasticity during FCG. The result can reproduce the major features of fatigue crack closure, the 3D and load-dependent evolution of PICC. Gonzales et al. [21] provided an experimental methodology to determine the reversed plastic zone size at the crack tip under cyclic loading through high-resolution digital image correlation (DIC) measurements.

Although modern X-ray microtomography 3D technology can achieve sub-micron resolution, cracks cannot be regarded as simple planar discontinuities in isotropic media, there is no direct method to measure the actual development of full-thickness crack closure, so the FEM is generally used in the study of RICC or OICC. Chen et al. [22] introduced elastic wedges into elastic cracks to simulate RICC or OICC effects and applied LEFM to solve the relationship between externally applied stress and crack opening displacement. Field et al. [23] conducted a general fractographic analysis of the fatigue fracture surface to understand what correlation there may be between surface roughness and the FCG rate. Gonzalez et al. [24] reviewed and discussed the key points on the RICC that are considered to affect crack tip shielding, the dislocation-based models have indicated that the crack tip shielding effect from a single asperity is relatively minor. Pippan et al. [25] explored the RICC effect from asymmetric dislocations and measured the local crystal orientation of fatigue cracks in the near-threshold region of Cu and Fe. Crapps et al. [26] studied the crack-closure problem under the combined action of PICC and RICC by introducing a serrated crack wake and changing the roughness and geometric shape period of the crack surface. The results show that the average crack closure degree increased with an increase in the roughness of the crack surface, whereas the geometric shape period has little effect on RICC. Pokluda et al. [27, 28] characterized the size of the crack-closure force component caused by roughness, the results are superior to the CJP model in evaluating the closure force component caused by roughness.

The FCG behavior in the mixed-mode has been further investigated since the introduction of compact tensile shear (CTS) specimens and relative loading devices by Richard [29]. Previous studies have reported that the effect of the L/r_p ratio (L and r_p represent the crack roughness length scale and plastic zone size, respectively) during a single peak overload may be similar to the RICC under constant amplitude (CA) loading [30, 31]. Parry et al. [32] studied the opening behavior of the crack tip section and the residual shear deformation of the asperity in the crack wake and described the crack deflection under CA loading from the perspective of micromechanics. Singh et al. [33] discussed and analyzed the competitive relationship between RICC and the PICC process after an overload. The material exhibited different degrees of deflection in mixed-mode loading conditions [34]. Under pure mode-I loading, FCG is not affected by RICC. However, under mixed-mode loading, it is affected by the mutual contact and interaction forces of the fracture surface. Previous work [35] showed that the crack propagation behavior

can be described more effectively because the solution includes PICC and RICC effects, compared with the traditional mixed model crack growth models with higher fitting correlation coefficients. The relevant studies of OICC are not described in this paper, because no redox reaction was found in the previous experiments, and no oxide accumulation was observed on the fracture surface.

The above studies are mainly devoted to exploring or explaining the mechanism of the PICC or RICC effect while proposing new means or using FEM and advanced technologies et al. to simulate the crack propagation process, and most of the studies focus on uniaxial loading conditions. Few literatures have described the interaction between PICC and RICC during crack deflection in the mixed-mode so far, so it is necessary to further study the crack closure effect in the process of crack deflection. In this study, EA4T axle steel was used to explore the variation of PICC and RICC under mixed-mode I + II loading conditions and the interaction between the two crack closure effects during crack deflection propagation. The DIC technique and the replica method were employed to record the crack tip displacement field, deflection angle and crack length, the change of SIFs during crack deflection was simulated by FEM.

2 Calculation of the Crack Closure

2.1 PICC Calculation

The CJP model established by Christopher et al. [36] considers the influence of compressive stress between crack surfaces and shear stress between crack sides, as shown in Figure 1, it shows the idealized diagram of the elastic-plastic interface stress at the crack tip during fatigue crack propagation (F_A is mode–I force; F_B is an additional force caused by mode–II loads; F_T is a force caused by positive T-stress; F_S is interface shear force in the elastic–plastic interval; F_C and F_P produce a shielding effect together; F_C is the contact force between the sides of the crack, and F_P is the force generated by the compatibility constraint of the plastically deformed material.). The crack tip plastic zone gradually transitions from the crack front to the crack wake with the crack propagation, a plastic inclusion is formed at the crack tip and a plastic wedge is formed between the crack sides to cause the PICC effect. The two effective crack propagation driving factors are used in the model, as shown in Eq. (1).

$$\begin{cases} \Delta K_{cjp} = (K_{F,max} - K_{R,max}) - (K_{F,min} - K_{R,min}), \\ \Delta K_F = K_{F,max} - K_{F,min}, \end{cases}$$

$$(1)$$

where K_F is the SIF that drives crack growth, and K_R is the SIF that acts to retard crack growth. $K_{F,max}$, $K_{R,max}$, $K_{F,min}$, $K_{R,min}$ at K_F and K_R under the maximum and minimum stress states.

The CJP model is defined as [36]:

$$\left| \sigma_y - \sigma_x + 2i\sigma_{xy} \right| = (A_r + i3B_i)z^{-\frac{1}{2}} + (B_r + iB_i)z^{-\frac{3}{2}}\bar{z} + Cz^0 + Dz^{-\frac{1}{2}}\ln(z) + Ez^{-\frac{3}{2}}\bar{z}\ln(z).$$

$$(2)$$

The elastic stress fields near the crack tip are given by:

$$\begin{cases} \sigma_y = \frac{1}{2}(A_r - 4B_r - 8E)r^{-\frac{1}{2}}\cos\frac{\theta}{2} + \frac{1}{2}B_r r^{-\frac{1}{2}}\cos\frac{5\theta}{2} + \\ \quad \frac{1}{2}B_i r^{-\frac{1}{2}}\left(\sin\frac{5\theta}{2} - \sin\frac{\theta}{2}\right) + \frac{1}{2}Er^{-\frac{1}{2}}\times \\ \quad \left[\ln(r)\left(\cos\frac{5\theta}{2} - 5\cos\frac{\theta}{2}\right) + \theta\left(\sin\frac{5\theta}{2} - 5\sin\frac{\theta}{2}\right)\right] + o\left(r^{\frac{1}{2}}\right), \\ \sigma_x = -\frac{1}{2}(A_r + 4B_r + 8E)r^{-\frac{1}{2}}\cos\frac{\theta}{2} - \frac{1}{2}B_r r^{-\frac{1}{2}}\cos\frac{5\theta}{2} - \\ \quad \frac{1}{2}B_i r^{-\frac{1}{2}}\left(\sin\frac{5\theta}{2} + 7\sin\frac{\theta}{2}\right) - \frac{1}{2}Er^{-\frac{1}{2}}\times \\ \quad \left[\ln(r)\left(\cos\frac{5\theta}{2} + 3\cos\frac{\theta}{2}\right) + \theta\left(\sin\frac{5\theta}{2} + 3\sin\frac{\theta}{2}\right)\right] - \\ \quad C + o\left(r^{\frac{1}{2}}\right), \\ \sigma_{xy} = -\frac{1}{2}r^{-\frac{1}{2}}\left(A_r\sin\frac{\theta}{2} + B_r\sin\frac{5\theta}{2}\right) + \\ \quad \frac{1}{2}B_i r^{-\frac{1}{2}}\left(\cos\frac{5\theta}{2} + 3\cos\frac{\theta}{2}\right) - \\ \quad Er^{-\frac{1}{2}}\sin\theta\left[\ln(r)\cos\frac{3\theta}{2} + \theta\sin\frac{3\theta}{2}\right] + o\left(r^{\frac{1}{2}}\right). \end{cases}$$

$$(3)$$

The K_F and K_R can be obtained in Eq. (4), which represent the driving SIF and the delaying SIF respectively.

$$\begin{cases} K_F = \lim_{r\to 0}\left[\sqrt{2\pi r}\left(\sigma_y + 2Er^{-\frac{1}{2}}\ln(r)\right)\right] \\ \quad = \sqrt{\frac{\pi}{2}}(A_r - 3B_r - 8E), \\ K_R = \lim_{r\to 0}\left(\sqrt{2\pi r}\sigma_x\right) = -4\sqrt{\frac{\pi}{2}}(2B_i + E\pi). \end{cases}$$

$$(4)$$

The five-parameter can be solved from displacement fields:

$$\begin{aligned} 2\mu & (u_x + iu_y) \\ & = \kappa\left(-2(B_r + iB_i)z^{\frac{1}{2}} - 2Ez^{\frac{1}{2}}\ln(z) - \frac{C}{4}z\right) - \\ & z\left(-(B_r + iB_i + 2E)\bar{z}^{-\frac{1}{2}} - E\bar{z}^{-\frac{1}{2}}\overline{\ln(z)} - \frac{C}{4}\right) - \\ & \left[(A_r + i3B_i)\bar{z}^{\frac{1}{2}} + D\bar{z}^{\frac{1}{2}}\overline{\ln(z)} - 2D\bar{z}^{\frac{1}{2}} + \frac{C}{2}\bar{z}\right], \end{aligned}$$

$$(5)$$

where u_x and u_y are the horizontal and vertical displacements respectively, $\mu = E/2(1+v)$; $k = 3-4v$ (plane

Wang *et al. Chinese Journal of Mechanical Engineering*   (2024) 37:81
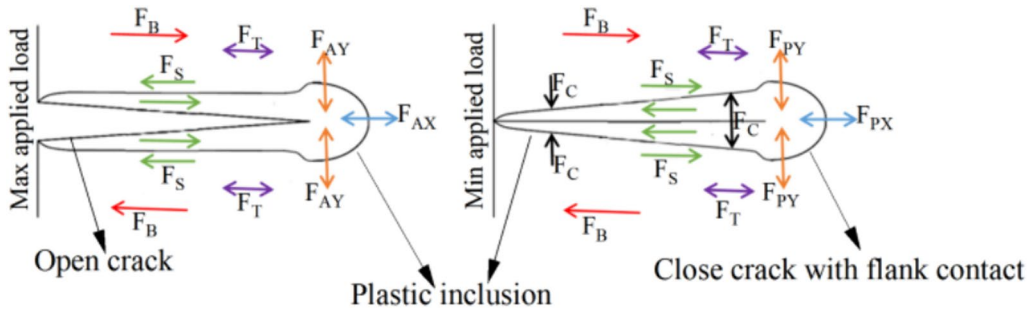
Page 4 of 15

Figure 1 Idealised diagram of crack tip elastic-plastic interface force

strain) or $k = (3−\nu)/(1+\nu)$ (plane stress); u_x and u_y are shown explicitly below with the assumption $D+E = 0$. After obtaining the crack tip displacement field, the equivalent stress value is solved according to the generalized Hooke's law. The value is compared with the yield strength value of the material to distinguish which stress values of the pixels obtained by DIC technology are in the linear elastic range. The position information of this part of the points is stored in the document. Substituting the displacement values of all points in the document into Eqs. (6) and (7), a linear equation set can be formed. The linear fitting method can be used to solve the parameters in the CJP model, and then the parameters such as K_F and K_R can be obtained.

$$
\begin{aligned}
2\mu u_x = {} & r^{\frac{1}{2}}(-A_r - 2B_r\kappa - 2E)\cos\frac{\theta}{2} \\
& + r^{\frac{1}{2}}(2B_i\kappa - 3B_i)\sin\frac{\theta}{2} + r^{\frac{1}{2}}(B_r + 2E)\cos\frac{3\theta}{2} \\
& - r^{\frac{1}{2}}B_i\sin\frac{3\theta}{2} - \frac{C}{4}r(1 + \kappa)\cos\theta \\
& + r^{\frac{1}{2}}E\ln(r)\left(\cos\frac{3\theta}{2} + (1 - 2\kappa)\cos\frac{\theta}{2}\right) \\
& + r^{\frac{1}{2}}E\theta\left(\sin\frac{3\theta}{2} + (1 + 2\kappa)\sin\frac{\theta}{2}\right),
\end{aligned}
\tag{6}
$$

$$
\begin{aligned}
2\mu u_y = {} & r^{\frac{1}{2}}(-2B_i\kappa - 3B_i)\cos\frac{\theta}{2} \\
& + r^{\frac{1}{2}}(A_r - 2B_r\kappa + 2E)\sin\frac{\theta}{2} + r^{\frac{1}{2}}(B_r + 2E)\sin\frac{3\theta}{2} \\
& + r^{\frac{1}{2}}B_i\cos\frac{3\theta}{2} + r^{\frac{1}{2}}E\ln(r)\left(\sin\frac{3\theta}{2} - (1 + 2\kappa)\sin\frac{\theta}{2}\right) \\
& - r^{\frac{1}{2}}E\theta\left(\cos\frac{3\theta}{2} + (1 + 2\kappa)\cos\frac{\theta}{2}\right) \\
& + \frac{C}{4}r(3 - \kappa)\sin\theta.
\end{aligned}
\tag{7}
$$

The crack closure ratio proposed by Pokluda [37] is

$$
\frac{K_{PICC}}{K_{\max}} \approx 2c,
\tag{8}
$$

where K_{PICC} is the SIF value calculated after considering PICC; $K_{\max}$ is the maximum SIF value; $c=b/10(\pi)^{0.5}B$; b is the distance between the upper and lower grains of the material, $B \approx 10^{-10}$ m; c is a dimensionless constant independent of the material, $c \approx 0.1$. It should be noted that the evaluation of PICC in the Pokluda model is relatively straightforward, requiring only certain material parameters for calculation. The listing of this expression is for analysis, comparison, and validation of the results obtained in this experiment.

In related studies, the load corresponding to crack opening is denoted as P_{op}, and U is used to represent the degree of crack closure [38, 39], as shown in Eq. (9). In this study, to quantify the PICC component, the $P_{op}/P_{\max}$ value is employed to represent the crack closure component. Based on the force-displacement data recorded during the experiment, combined with the parabolic-linear method [40], the crack opening force at each stage of crack deflection can be determined.

$$
U = \frac{P_{\max} - P_{op}}{P_{\max} - P_{\min}},
\tag{9}
$$

where U is a dimensionless constant; $P_{\max}$ and $P_{\min}$ are the maximum and minimum load, respectively.

2.2 RICC Calculation

The asymmetry of dislocations and roughness of the fracture surface led to different shear displacements on both sides of the crack, resulting in the RICC effect. Assuming that the roughness geometry is simple, as shown in Figure 2, the dotted line indicates the crack propagation direction. The calculation expression is given in Eq. (10) [27].

$$
\frac{K_{RICC}}{K_{\max}} = C\eta\sqrt{(R_A^2 - 1)} + \frac{3\eta(R_A - 1)}{2\sqrt{6} + 6(R_A - 1)}
\tag{10}
$$

$$\eta = \left[-\left(\frac{0.866 S_{Rc} r_p}{d_m} \right)^{2.2} \right] \tag{11}$$

where K_{RICC} is the RICC SIF; $K_{\max}$ is the maximum SIF, and R_A is the roughness of the fracture. η is a statistical parameter, it obeys the Weibull distribution. $S_{\mathrm{Rc}} \in (0.2,1)$ is a fitting parameter, and a value of 0.5 is generally acceptable [41]. d_m is the characteristic microstructure distance, and r_p is the static plastic zone size [28].

A theoretical analytical solution of the CJP model in mixed-mode is presented in the previous work, as shown in Eq. (12). The crack deflection propagation behavior can be described more effectively by considering the influence of PICC and RICC [35]. The SIF value in the process of crack deflection is calculated by Eq. (12) in this study.

$$\begin{cases} \Delta K_{P-R} = x \left(K_{F,\max} - K_{R,\max} \right) - \left(K_{F,\min} - K_{R,\min} \right), \\ x = 1 - C\eta \sqrt{R_A^2 - 1} - \dfrac{3\eta (R_A - 1)}{2\sqrt{6} + 6(R_A - 1)}, \end{cases} \tag{12}$$

where $\Delta K_{\mathrm{P\text{-}R}}$ is the ΔK_{eff} value with the consideration of PICC and RICC effects, and x is the linear scaling factor. R_A value can be obtained by measuring the fracture area after the testing.

3 Experimental Procedure

The sample material used in this study was EA4T axle steel. The specimens were subjected to a mixed-mode I + II loading FCG test, which was performed using an electronic tensile-torsion testing machine (INSTRON E10BMT). For the formal test, $P_{\max} = 4$ kN, $R = 0.1$, and $f = 25$ Hz, and CA loading was carried out in the directions of 30°, 45°, and 60°. During the test, a replica method was adopted to record the crack propagation trajectory, so the crack tip location and angle can be defined after a certain number of cycles. The crack propagation length was measured after a specific number of cycles, and loaded at a low speed (the maximum load remained unchanged). The sampling frequency was adjusted to
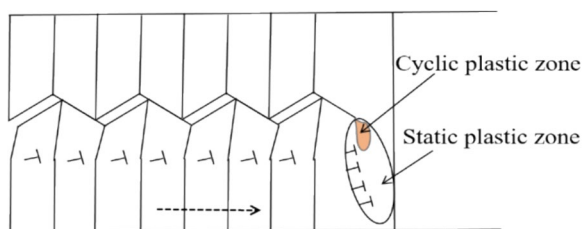

Figure 2 Diagram of maximum long-range RICC induced by asymmetric dislocation array

1000 Hz to collect sufficient load-displacement data. A DIC device, i.e., Revealer 2D-DIC was used to obtain the displacement field of the FCG and calculate the change in the SIF value at the crack tip during crack deflection. The resolution of DIC equipment is 0.00638 pixels/mm. An industrial microscope with a resolution of 10 μm was used to observe and record crack propagation paths in real-time.

The fatigue crack propagation process in the mixed-mode can be divided into two stages. In the first stage, under the interaction of shear and tensile stresses perpendicular to the prefabricated crack surface, cracks initiated and propagated in the surface slip band under shear stress. In the second stage, crack propagation was approximately perpendicular to the principal tensile stress, as shown in Figure 3a. As the crack propagated from the prefabricated crack position to the first stage of crack propagation, the slip system formed a certain angle with the crack propagation direction, resulting in crack deflection. The mixed-mode loading device and crack deflection are shown in Figure 3a, the fixture designed by Richard was employed for loading [29]. The dimensions of the specimen are shown in Figure 3b, and the field test device is shown in Figure 4. The chemical compositions and basic mechanical properties of the materials are listed in Tables 1 and 2, respectively, where Et. is element, Wt. is weight (%). E is elastic modulus (GPa), ν is poisson's ratio, σ_s is yield strength, σ_b is tensile strength (MPa), δ is elongation (%), Ψ is reduction of area (%) [42]. It is worth noting that the degradation phenomenon of material mechanical properties is not considered in this study, mechanical properties, such as yield strength, ultimate tensile strength and elongation are key factors in damage evaluation. Sun et al.'s work showed that the degradation of mechanical properties is influenced by cyclic softening/hardening characteristics of materials, and a comprehensive characterization method is proposed using a tensile plastic strain energy density parameter [43].

4 Results and Discussions
4.1 Simulation Results

The research shows that the FEM is used to simulate the crack propagation process, which can reflect the change trend and range of each parameter to a certain extent. In Singh et al's work [33], a single crack deflection angle of $\theta = 45°$ and deflection lengths between $L = 18.75$ and $L = 225$ μm are considered, fatigue surface roughness is idealized as a simple regular zigzag geometry for RICC studies. This modelling method is convenient for researchers to explore the changing trend of the RICC effect, but the crack deflection angle is fixed, while the crack deflection angle of the material or structure in service is changed in real time. In Nittur et al's work [44], only the right half of the specimen is modelled due to symmetries of the loading and geometry
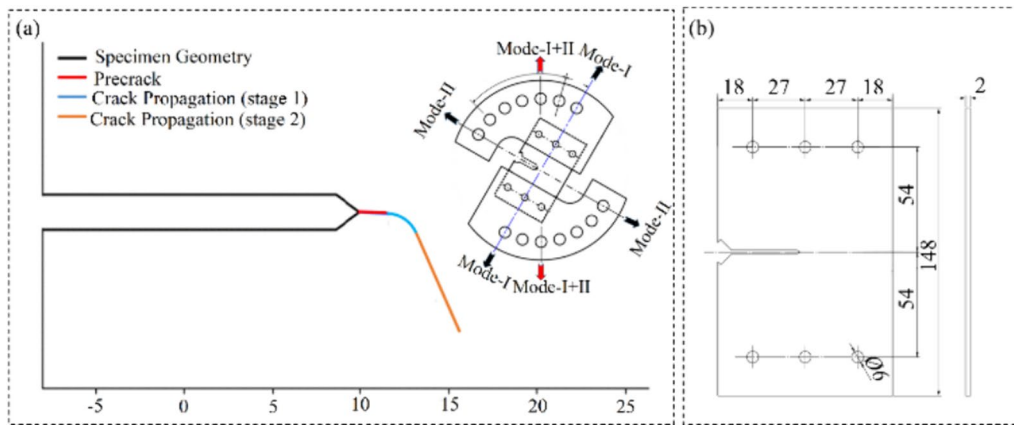
Figure 3 Crack deflection and test loading diagram: **a** crack deflection stage and fixture, **b** geometric dimensions of CTS specimen
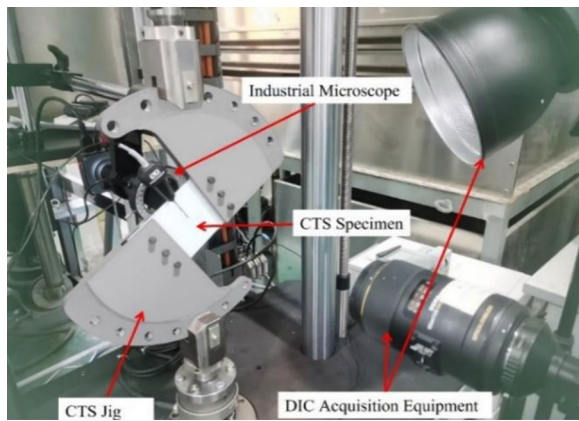

Figure 4 Test device (loading angle α=60°)

and appropriate boundary conditions are imposed along the vertical symmetry line. The model consists of 16 layers of 8 noded isoparametric 'C3D8R' brick elements and has finer mesh towards the free surface and coarser mesh towards the mid-plane. The crack propagation is accomplished by releasing the constraints on the current crack front nodes at the end of the load cycle. Since the crack deflection occurs during the mixed-mode crack propagation process, the submodel technique was not used in this study. In Antunes et al's work [45], the finite element mesh is refined at the crack front to model the severe plastic deformation gradients and enlarged at remote positions to reduce the numerical effort. In this study, the model crack

propagation path element was also preprocessed to reasonably simulate the crack propagation process.

In this study, a commercial finite element software Franc3D 8.0 was used to simulate FCG in mixed-mode. The element type was selected as an 8-node isoparametric plane stress element (CPS8 element). According to Richard distribution equation [46], the CTS specimens were subjected to force and constraint. It is worth noting that in the study of elastic-plastic stress (strain), simulation results are influenced by the loading path when plastic stress/deformation is involved. For instance, if tensile loading is applied before shear loading or shear loading is applied before tensile loading, the results can differ significantly [47, 48]. The above problems are avoided by using the Richard distribution equation for loading and constraint setting.

CTS modelling was established in the finite element software of HyperWorks 21.0. The cell grid was divided into three parts based on its size: the first part was a circular area with a diameter of 14 mm centred on the crack tip. Based on the sensitivity analysis results of Wang et al. [34], the cell grid size of this part was 0.05 mm. The grid size increases from the inside to the outside, and the other two parts of the grid size are 0.1 mm and 0.2 mm, respectively, as shown in Figure 5. Material parameters were set according to the values provided in Table 2, and Paris constants were determined based on experimental fitting results, with $c = 4.92 \times 10^{-9}$ and $m = 2.1676$ [35]. A 2 mm elliptical crack at the initial crack tip throughout the entire thickness of the CTS

Table 1 Chemical composition of EA4T (%)

Et.	C	Si	Mn	P	S	Cr	Cu	Ni	Mo
Wt.	0.27	0.39	0.72	0.0075	0.0013	1.11	0.014	0.25	0.247

E	v	σ_s	σ_b	δ	Ψ
209	0.3	520	695	20.88	63.76

specimen was inserted. Subsequently, a combination of the extended finite element method (XFEM) was used to simulate mixed-mode crack propagation. This study calculated the SIF based on the displacement extrapolation method [49], as shown in Eq. (13).

$$\begin{cases} K_I = \lim_{r \to \infty} 0.25E(2\pi/r)^{0.5}u_2, \\ K_{II} = \lim_{r \to \infty} 0.25E(2\pi/r)^{0.5}u_1, \end{cases} \quad (13)$$

where E is Young's modulus, r is the distance from the crack tip, u_1 and u_2 are the opening displacement and sliding displacement of the two relative points above and below the crack.

The maximum tangential stress (MTS) [50] and strain energy density factor (S) criteria [51] were sat as the mixed-mode crack growth criterion in this paper, the theoretical expressions of crack propagation direction θ of MTS criterion and S criterion are shown as follows:

MTS criterion:

$$\theta = \arccos \frac{3K_{II}^2 + \sqrt{K_I^4 + 8K_I^2 K_{II}^2}}{K_I^2 + 9K_{II}^2}, \quad (14)$$

S criterion:

$$\frac{\partial S}{\partial \theta} = 0 \text{ and } \frac{\partial^2 S}{\partial^2 \theta} > 0, \quad (15)$$

where S is the strain energy density coefficient, $S = a_{11}K_I^2 + 2a_{12}K_I K_{II} + a_{22}K_{II}^2$, the coefficients $a_{11} = (1+v/8\pi E)(1+\cos\theta)(k-\cos\theta)$, $a_{12} = (1+v/8\pi E)\sin\theta[2\cos\theta-(k-1)]$, $a_{22} = (1+v/8\pi E)[(k+1)(1-\cos\theta)+(1+\cos\theta)(3\cos\theta-1)]$. E and v are Young's modulus and Poisson's ratio, respectively, $k = (3-v)/(1+v)$ under plane stress condition and $k = 3 - 4v$ under plane strain condition.

As there was a small difference between the calculated values of the two criteria in previous work, only the MTS results were plotted here, as shown in Figure 6. The variation in K_I and K_{II} values with crack length is depicted in the figure, K_I and K_{II} are the SIF values of mode-I and mode-II loading conditions, respectively. In Figure 6a, with increased crack propagation length, the K_I value shows an overall upward trend, consistent with the results obtained using the Westergaard method. The curve in Figure 6a showed an alternating trend of increase and decrease during ascent, which was related to crack deflection. The a–b segment in Figure 6b is defined as the first stage and the b–c segment is defined as the second stage, the dotted line is the fitted line of the simulation data, which has no clear physical meaning for the following analysis. The K_{II} value gradually increased with increasing crack length in the first stage and decreased in the second stage. The growth trend of the K_{II} value in the first stage was similar to that of the Paris crack propagation curve. As the crack length increased, the contact area of the crack side also increased. In combination with the crack deflection diagram in Figure 3a, the variation
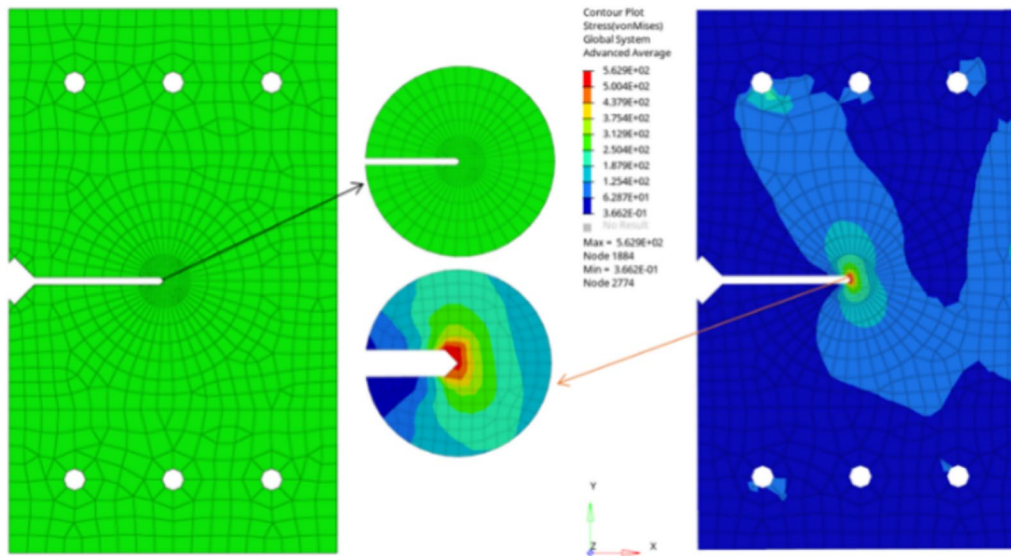

Figure 5 Exemplary FEA results of mixed-mode loading (*a* = 45 °)

Wang *et al. Chinese Journal of Mechanical Engineering*   (2024) 37:81

Page 8 of 15

trend of K_{II} value is explained. As shown in Figure 7, P_I and P_{II} are the loads corresponding to the directions perpendicular and parallel to the crack propagation, the a-c in Figure 7 shows the load projection when the mixed mode's loading angle is set to 30 °, 45 ° and 60 ° respectively. The first stage region in Figure 3a was non-contact in the mixed-mode loading when the crack propagated, and as the crack deflected (the stages 1 to 2), although the P_{II} value increased to the maximum load of the loading cycle, the P_I value hindered the slip-effect of the P_{II} value parallel to the crack propagation direction and the K_{II} value eventually stabilized as the crack continued to propagate, as shown at point *c* in Figure 6b. Due to the micro-geometric structure of the material and the influence of inclusions and defects in this process, the crack propagation path changed slightly, but the overall propagation path direction was approximately perpendicular to the loading axis.

Before analyzing the variation of SIFs during the crack deflection process, it is essential to understand how the applied load is projected into the directions parallel and perpendicular to the crack propagation under mixed-mode conditions. This is crucial for gaining a clear insight into the changes in SIFs in Figure 6. With an increase in the initial loading angle, the P_I value decreased, and the P_{II} value increased. The variation in crack deflection angle leads to changes in the projected loads in different directions, P_I and P_{II} interact with each other in this process. The presence of P_I hinders the slip effect parallel to the crack propagation direction caused by P_{II}, while the presence of P_{II} results in the deflection of the crack propagation direction. P_I and P_{II} dominated the variation trends of K_I and K_{II}, the final manifestation of the competitive relationship between P_I and P_{II} was the competitive relationship between K_I-dominated PICC and K_{II}-dominated RICC. The results indicated that the crack deflected in
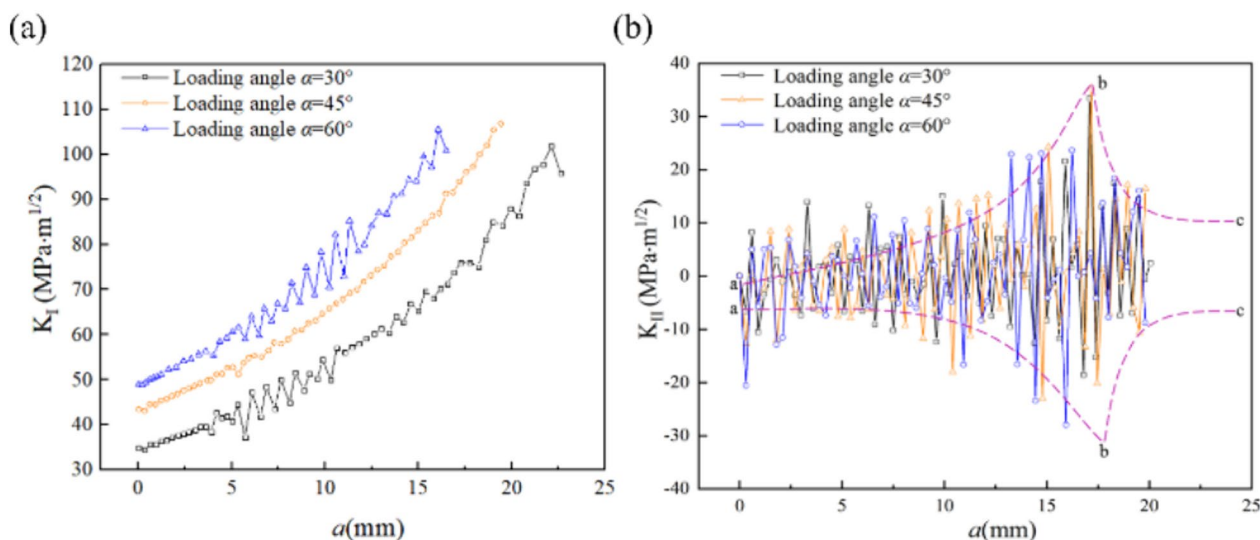

Figure 6 Relationship between K_I, K_{II} and distance along crack propagation path with different loading angles (R=0.1): **a** a-K_I, **b** a-K_{II}
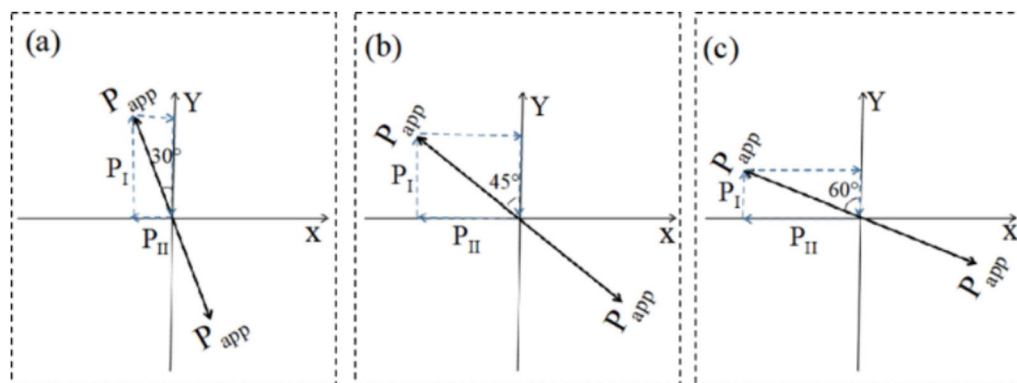

Figure 7 Loading force decomposition diagram with different loading angles: **a** a=30°, **b** a=45°, **c** a=60°

Wang *et al. Chinese Journal of Mechanical Engineering*   (2024) 37:81

Page 9 of 15

the first expansion stage and the crack propagation direction was perpendicular to the loading axis in the second.

The alternating effect of the loading angle $\alpha=45°$ in Figure 6a was not apparent compared with other loading angles, and the reason for this result was analyzed. Under the initial condition of $\alpha=45°$, the values of P_I and P_{II} were equal, as shown in Figure 7b, and the crack deflected after a certain number of cycles. Although RICC has an effect on the PICC during the deflection process, the effect of the interaction was not significant due to the same magnitude of the load, so the peak value of K_{II} at $\alpha=45°$ in the first stage of Figure 6b was significantly lower than that at the other two angles. In addition, the mean value of K_{II} value under three loading angles in the range of 2–5 mm was maintained at the same level, because the crack deflect needs to undergo a certain number of cycles.

4.2 Experimental Results

The roughness values (R_A) on both sides of the crack in the fatigue crack propagation test were measured by the optical microscope (Atometrics ER230) after the test, and the crack roughness-induced closure scale was analyzed and calculated. In addition, the fracture morphology was analyzed by SEM (JSM 7800F). When measuring the roughness of the fracture surface, the fracture surface area is divided into four regions ((a)–(d)) according to the Paris crack propagation curve division method, which represents the prefabricated crack, low-speed, medium-speed, and high-speed propagation areas, respectively, as shown in Figure 8a-d.

The crack surface R_A was measured, as shown in Figure 9a-d, the coordinate axes x and y represent the measurement range of roughness measurement. The measurement results in Figure 9a-d are derived from the corresponding positions in the region outlined in Figure 8a-d. The size of the measured fracture surface area is 900×500 μm. The result showed that the surface roughness on both sides of the crack gradually increased with crack propagation. The RICC value can be obtained by substituting the measurement results into Eq. (10). The reason for the change of roughness in Figure 9 is that the fatigue fracture surface contacts during the crack deflection process. Under the action of cyclic load, the friction of the contact surface leads to the increase of the roughness value of the fracture surface.

The calculation results of PICC and RICC obtained from the test are plotted in Figure 10. The overall level of the PICC value in Figure 10(a) was approximately 0.2, which was consistent with the theoretical calculating values of Eq. (8). However, the PICC value in the curve was not fixed at a certain value, and the PICC curve extended in a wavy manner. The final crack closure degree P_{op}/P_{max}
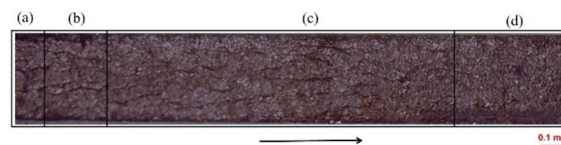

Figure 8 Fracture surfaces under mixed-mode (R=0.1, α=45°): **a** prefabricated crack stage, **b** initial crack deflection stage, **c** crack deflection stage, **d** end stage of crack deflection

tended to be constant at approximately 0.2, it was similar to the calculation results of Wang et al. [34] and Lu et al. [38]. The results from Wang et al. [34] also indicate an inconsistent trend in the P_{op}/P_{max} variation between the base material and the welded joint. This inconsistency is attributed to the fact that residual stresses in the weld are not eliminated through post-weld heat treatment. As the crack propagates, the P_{op}/P_{max} decreases and gradually stabilizes. Since the material used in this test was EA4T base metal, the crack closure trend of the material after welding was not studied.

The abscissa in Figure 10b represents the experimentally measured fracture surface R_A, while the ordinate represents the RICC results corresponding to different R_A. The four measuring points in Figure 10b correspond to the pre-crack, the initial crack deflection, the middle crack deflection and the end of the crack deflection stage. A/B/C/D is used to represent the four stages for the convenience of analysis and description. The variation range of R_A from stage B to C was significantly narrower than the stage A to B in Figure 10b, it was the result of the interaction between the PICC and RICC. The interaction or competition between the two closure effects aggravates the contact between the crack fracture surfaces, resulting in a large change in the R_A value of the fracture surface. The RICC value presented in Figure 10b was illustrated by combining the simulation results shown in Figure 6b. The K_{II} value provides the driving force for RICC, and the RICC effect was correspondingly enhanced with the increase of K_{II}. After the crack propagation entered stage D, the crack deflection ended and the crack propagation direction was approximately perpendicular to the loading axis. The change after stage D was not analyzed and discussed, as this study focuses on the crack deflection process under mixed-mode loading.

Figure 11 shows the recorded results of the fatigue crack growth rates (FCGR) during the experimental process: the FCGRs showed an overall upward trend, and there was also an alternating pattern of increase and decrease in the early stages of crack propagation. This trend was consistent with the results in Figure 6a, where K_I values act as the driving force for crack propagation
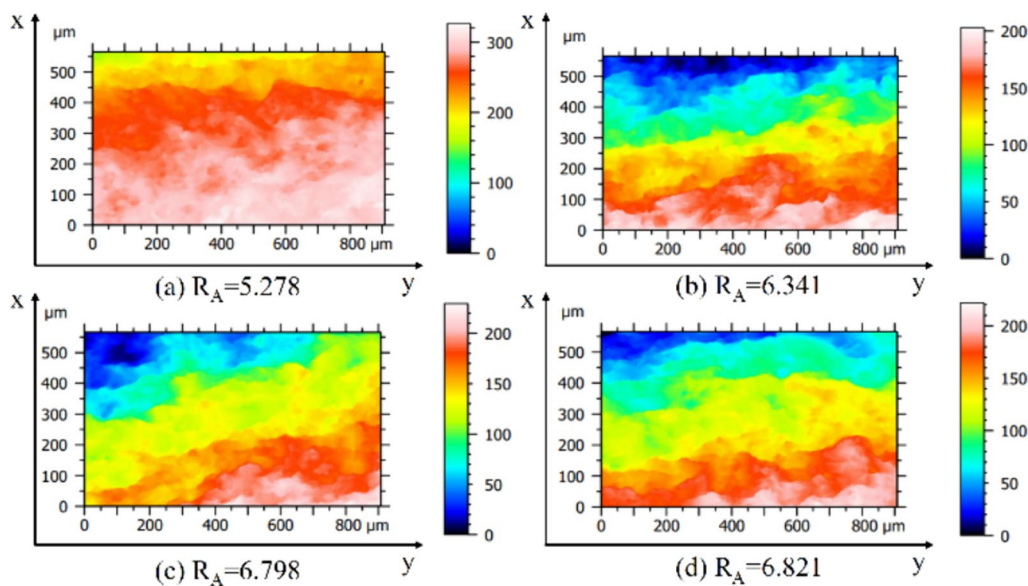
Figure 9 Crack surface roughness measurement results (R=0.1, α=45°): **a** prefabricated crack stage, **b** initial crack deflection stage, **c** crack deflection stage, **d** end stage of crack deflection
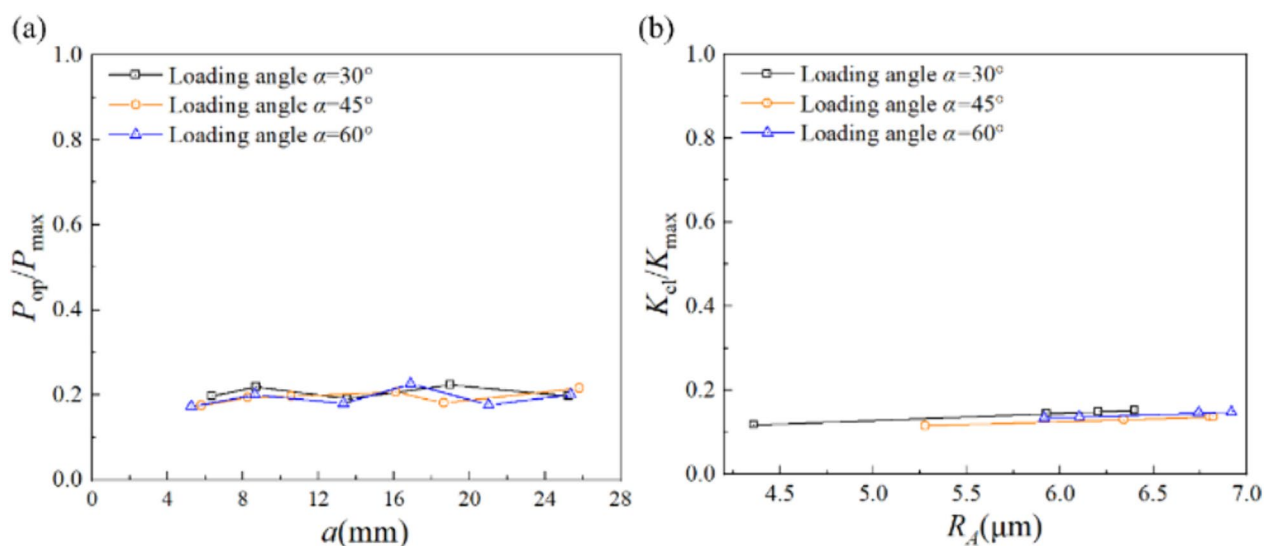

Figure 10 Crack closure level with different loading angles: **a** PICC value, **b** RICC value

and PICC. The alternating changes in K_I values contribute to the alternating pattern in FCGRs.

4.3 Discussions

Based on the above simulation and experiment, the authors surveyed relevant studies on crack closure under mixed-mode conditions. Partial experimental results were presented to conduct a comparative analysis with the findings of this study. Zhang et al's [52] simulation results show that the crack closure level under the plane stress state is about 0.4, and the results are consistent with the estimated level of Eq. (8). The closure ratio in plane stress conditions is 2–2.5 times that in plane strain conditions, the calculated PICC average value of this test was 0.2, the experimental results in the plane strain state have the same trend as the above results. Furthermore, it was observed that as the stress ratio increased from 0.1 to 0.3, the degree of crack closure increased. This is
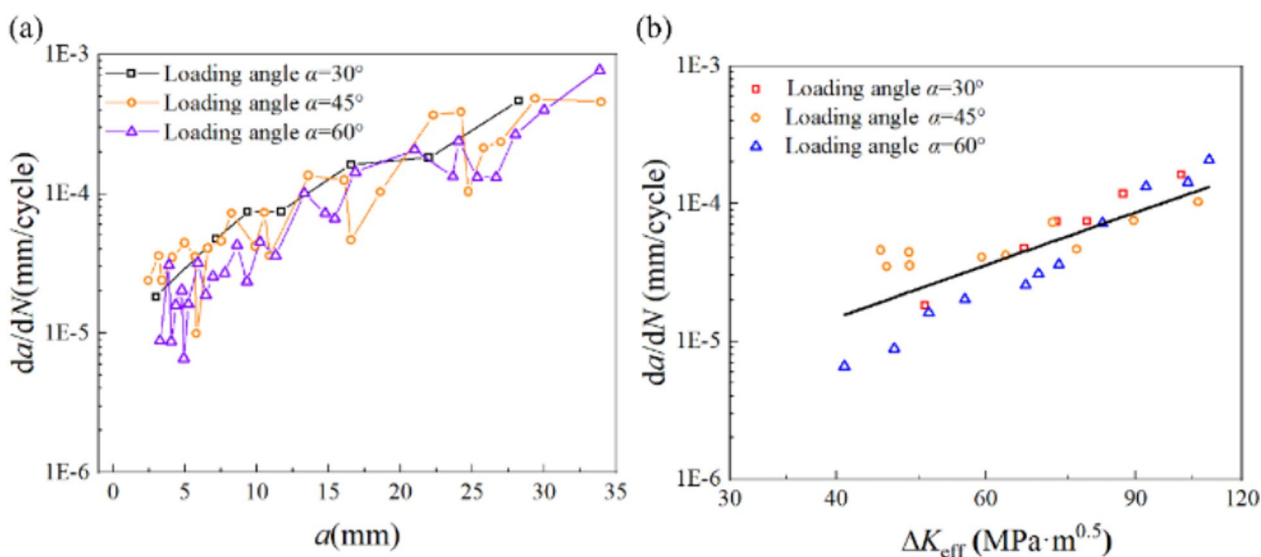
Figure 11 Test record result: **a** a-da/dN, **b** ΔK_{eff}-da/dN

attributed to the increase in $P_{\min}$ in the denominator of Eq. (9). A higher stress ratio means that the loading minimum load $P_{\min}$ increased, and the denominator in Eq. (9) decreased resulting in a significant upward shift of the crack closure level.

The FCG behaviors of Al-Li-Cu-Mg alloy (8090) and traditional Al-Cu-Mg alloy (2004) are compared in a study by Rodrigues et al. [39]. The crack closure level of Al-2024 is in the range of 0.4–0.6, but the crack closure level of Al-8090 alloy is 0.7–0.9, the reason is that the fracture analysis results of Al-8090 alloy indicated a transgranular fracture mode (high roughness, high crack deflection), it is characteristic of extensive crack closure caused by the roughness wedge. Suresh et al. [53] proposed the RICC geometric model of a fracture surface and considered the contribution of the crack tip displacement of modes I and II in early research. The results show that the displacement ratio is positively correlated with the crack closure level. The crack closure level corresponding to the test data of the two materials (Rail steel and 1018 steel) is approximately 0.4, which is of the same order of magnitude as the crack closure level of the PICC under CA in Eq. (8). The material used in this experiment was EA4T steel, which exhibits consistency in crack closure behavior with the material properties used in Suresh's experimental study.

The crack deflected in the prefabricated direction follows the same mechanism as the composite direction of the force defined in physics under mixed loading, as illustrated in Figure 7. As the deflection angle changes, the projected values onto the X and Y axes change accordingly. The plastic zone at the crack tip caused by angle

deflection was a butterfly asymmetric structure. The asymmetric structure leads to crack propagation along the smaller side of the plastic zone. The crack propagation rate was slowed down because the load in the crack tip region generated the residual compressive stress. When the crack is deflected, the constraint of the crack along the propagation direction is reduced due to the smaller load projected onto mode-II. At this moment, the crack propagation along the single-slip system was dominated by mode-I load, resulting in a jagged crack propagation path. The contact area of the serrated crack propagation path increased as the load projected onto mode-II increased and the crack deflection progressed. The crack tip was passivated under cyclic loading, and the ratio of P_{op} to $P_{\max}$ approximately represented the PICC value. The presence of RICC caused the crack side to make contact in advance, resulting in a small P_{op} value in the subsequent loading cycle. The change in P_{op} was positively correlated with the PICC value, thus the PICC value fluctuates under cyclic loading. After crack deflection was completed, the crack propagation direction was approximately perpendicular to the loading axis. The crack propagation can be approximated as mode-I crack propagation, the PICC value tends to be a fixed value now, as shown in the latter half of the curve in Figure 10a. Moreover, the degree of crack closure was negatively correlated with the test loading angle, consistent with similar findings reported in Ref. [52].

As the contact area of the serrated crack propagation path increased, the contact friction between the fracture surfaces caused a larger R_{A} value in the contact area, as described in the calculation expression of the RICC value
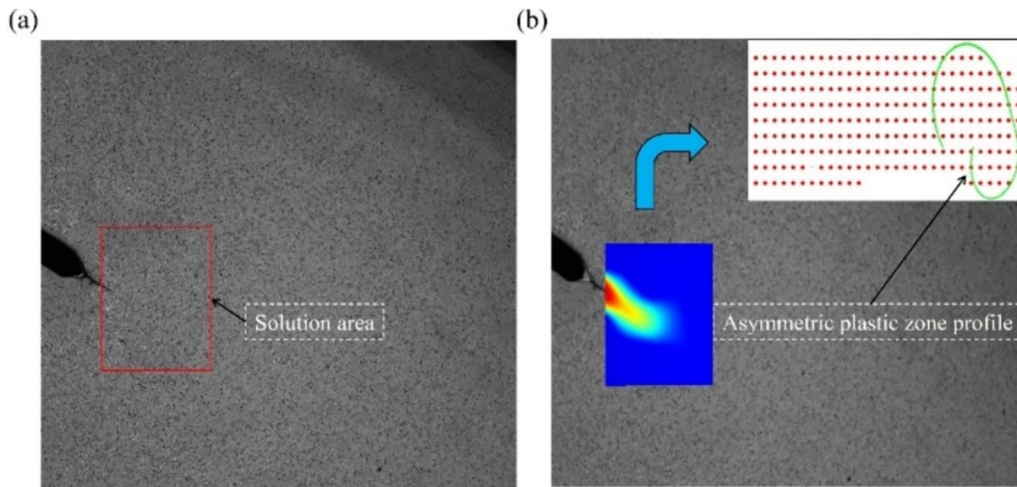
Figure 12 Deflection diagram of plastic zone at crack tip (*a*=30°, *a*=7.152mm): **a** test image obtained by DIC; **b** shape of plastic zone at crack tip
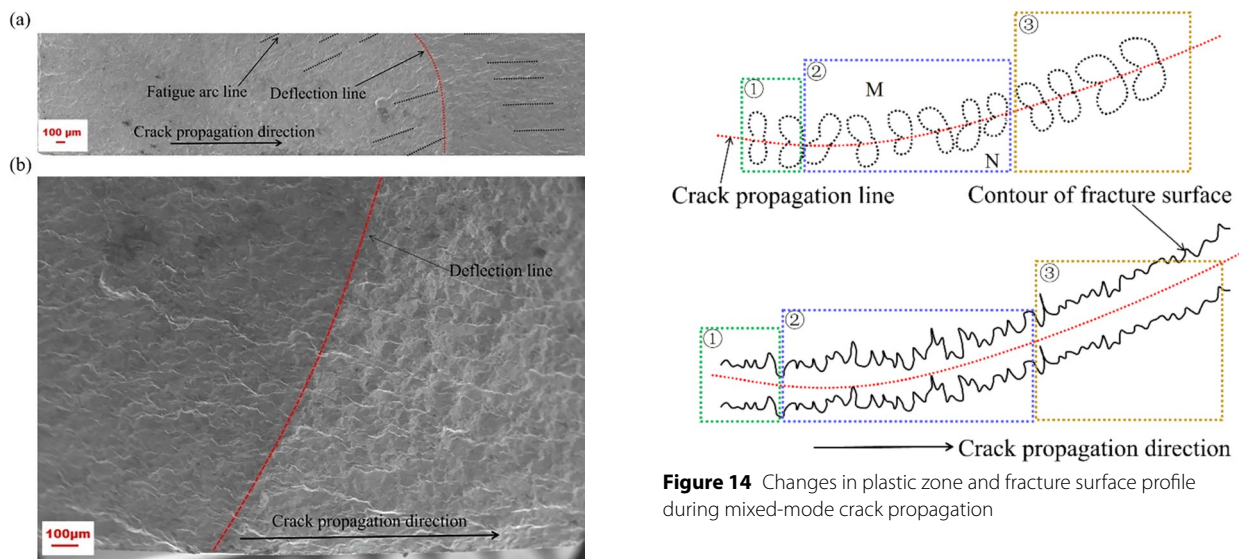

Figure 13 Mixed-mode loading fracture surface (*a*=30°): **a** macro schematic diagram, **b** partial enlargement diagram

Figure 14 Changes in plastic zone and fracture surface profile during mixed-mode crack propagation

in Eq. (10). The RICC value shows a positive correlation with R_A value. The RICC values obtained from the test results were plotted in Figure 10b, demonstrating an approximately linear relationship with the R_A value, with the RICC value being around 0.15. The crack tip displacement field was obtained by the DIC technique, and then the plastic zone at the crack tip was calculated using the Tresca yield criterion, the position of the solution area is shown in Figure 12a. During the crack deflection process, the plastic zone at the crack tip exhibited an asymmetrical butterfly shape, as shown in Figure 12b.

The larger side of the plastic zone at the crack tip facilitated the elastic recovery of the plastic inclusion when the load was at its minimum, which led to a decrease in the distance between the plastic wakes on both sides of the crack [54]. However, due to the serrated propagation path of the crack, the upper and lower fracture surfaces are contacted in advance during the elastic recovery stage hindering the PICC process.

The fracture surface of the specimen was analyzed using SEM at the end of the test, as shown in Figure 13. Figure 13 shows the macroscopic schematic of the mixed-mode fracture surface and the local amplification diagram of the crack deflection line position, respectively. In Figure 13a, the black arrow indicates

the crack propagation direction, the fracture surface was rough and had no metallic lustre. The fatigue arc and crack deflection line angle were approximately 25°, and the crack deflection angle was approximately 30°. Notably, the roughness of the crack surface before and after crack deflection was different, the roughness of the crack surface before crack deflection was smooth, as shown in Figure 13b. The crack formed a symmetrical butterfly-shaped plastic zone at the crack tip under mode-I loading. Owing to the mixed-mode loading conditions, irreversible residual shear deformation was introduced at the crack tip, and a spatially torsional crack surface was formed during crack propagation.

During the crack propagation process, the shape of the plastic zone changed due to contact with the crack surface. The alterations in the plastic zone and fracture surface profile before and after crack deflection in the mixed-mode are illustrated in Figure 14, where ① – ③ represents the prefabricated crack stage, the crack deflection stage, the stage with crack propagation direction perpendicular to the loading axis, respectively. Crack deflection occurred in the second stage, the plastic zone at the crack tip was asymmetric during the deflection process. The crack propagation line was used as the dividing line, and the area of the plastic zone at the crack tip in the M and the N regions changed alternately. The results of the interaction between PICC and RICC during crack deflection were again confirmed.

Considering the influence of fracture surface roughness on crack propagation rate, from the findings in this work, the evolution law of the fracture surface roughness is explored in the following work, and the parameters of the fracture surface roughness evolution are set onto the mixed-mode crack growth path, and the crack growth process can be obtained by combining the XFEM method. It is worth mentioning that the specimen is always in a tensile state under a high-stress ratio, and the crack closure effect will be affected by the stress ratio, which is also the influencing factor to be considered in future work.

5 Conclusions

(1) The driving force of the PICC and RICC is the K_{I} and K_{II}, the K_{I} and K_{II} values in the mixed-mode increased with crack propagation, and the latter then decreased to a stable value. The reason for this decrease is that the crack propagation direction gradually becomes perpendicular to the loading axis after crack deflection, the mixed-mode loading can be approximated as mode-I loading at this moment. The P_{I} value hindered the slip effect of the P_{II} value parallel to the crack propagation direction during the process of crack deflection.

(2) The interaction relationship between K_{I} and K_{II} values during crack deflection slowed the crack propagation rate to a certain extent. After crack deflection, the crack propagation rate increased linearly. The asymmetric butterfly-shaped plastic zone at the crack tip caused by crack deflection facilitated crack propagation along the smaller side of the plastic zone.

(3) The value of the PICC result was fluctuation due to early contact with the crack surface caused by RICC. The serrated crack propagation path hindered the elastic recovery of the plastic inclusion at the crack tip when the load was at its minimum. The result of the interaction between PICC and RICC was that the variation in roughness caused by contact friction between the fracture surfaces was slowed.

(4) The roughness difference of the crack surface before and after crack deflection was obvious. Owing to the mixed-mode loading, irreversible residual shear deformation was introduced at the crack tip, and a spatially torsional crack surface was formed during crack propagation. The changing trend of the crack tip plastic zone area was consistent with the changing trend of the fracture surface profile roughness, the plastic zone at the crack tip was asymmetric during the deflection process.

Data availability
Date will be available from the corresponding author on reasonable request.

Declarations

Competing Interests
The authors declare no competing financial interests.

Wang *et al. Chinese Journal of Mechanical Engineering*   (2024) 37:81

Page 14 of 15

References

[1] F Bjørheim, S C Siriwardane, D Pavlou. A review of fatigue damage detection and measurement techniques. *International Journal of Fatigue*, 2022, 154: 106556.

[2] T Oplt, T Vojtek, R Kubíček, et al. Numerical modelling of fatigue crack closure and its implication on crack front curvature using $\Delta CTOD_p$. *International Journal of Fatigue*, 2023, 171: 107570.

[3] B Yang, S Wang, J Li, et al. Crack growth behavior of U71MnG rail steel under overload conditions described using a dislocation correction mode. *International Journal of Fracture*, 2024, 1-15.

[4] D Kujawski, A K Vasudevan, R E Ricker, et al. On 50 years of fatigue crack closure dispute. *Fatigue & Fracture of Engineering Materials & Structures*, 2023, 46(8): 2816-2829.

[5] P Zhang, L Xie, C Zhou, et al. Experimental and numerical investigation on fatigue crack growth behavior of commercial pure titanium under I-II mixed mode loading at negative load ratios. *International Journal of Fatigue*, 2020, 138: 105700.

[6] Z S Hosseini, M Dadfarnia, B P Somerday, et al. On the theoretical modeling of fatigue crack growth. *Journal of the Mechanics and Physics of Solids*, 2018, 121: 341-362.

[7] S Qi, L X Cai, C Bao, et al. Analytical theory for fatigue crack propagation rates of mixed-mode I–II cracks and its application. *International Journal of Fatigue*, 2019, 119: 150-159.

[8] Y Z Li, S P Zhu, D Liao, et al. Probabilistic modeling of fatigue crack growth and experimental verification. *Engineering Failure Analysis*, 2020, 118: 104862.

[9] S Stoychev, D Kujawski. Methods for crack opening load and crack tip shielding determination: a review. *Fatigue & Fracture of Engineering Materials & Structures*, 2003, 26(11): 1053-1067.

[10] M Skorupa. Load interaction effects during fatigue crack growth under variable amplitude loading- a literature review. Part II: qualitative interpretation. *Fatigue & Fracture of Engineering Materials & Structures*, 1999, 22(10): 905-926.

[11] M L Z, J Long, F Z Xuan. Fatigue life and mechanistic modeling of interior micro-defect induced cracking in high cycle and very high cycle regimes. *Acta Materialia*, 2018, 157:259-275.

[12] W H Peters, W F Ranson. Digital imaging techniques in experimental stress analysis. *Optical Engineering*, 1982, 21(3): 427-431.

[13] I Yamaguchi, T Furukawa, T Ueda, et al. Accelerated laser speckle strain gauge. *Optical Engineering*, 1986, 25(5): 671-676.

[14] R C McClung. Crack closure and plastic zone sizes in fatigue. *Fatigue & Fracture of Engineering Materials & Structures*, 1991, 14(4): 455-468.

[15] C J Christopher, M N James, E A Patterson, et al. Towards a new model of crack tip stress fields. *International Journal of Fracture*, 2007, 148: 361-371.

[16] C J Christopher, M N James, E A Patterson, et al. A quantitative evaluation of fatigue crack shielding forces using photoelasticity. *Engineering Fracture Mechanics*, 2008, 75(14): 4190-4199.

[17] B Yang, Z Wei, F A Diaz, et al. New algorithm for optimised fitting of DIC data to crack tip plastic zone using the CJP model. *Theoretical and Applied Fracture Mechanics*, 2021, 113: 102950.

[18] J Li, B Yang, S Wang, et al. Modified model of crack tip stress field considering dislocation slip accumulation and crack tip blunting. *Chinese Journal of Mechanical Engineering*, 2023, 36(1): 47.

[19] B Yang, S Wang, J Li, et al. Study on fatigue crack growth in rail steel at numerical and experimental approaches. *Materials*, 2023, 16(8): 2981.

[20] F Paysan, E Breitbarth. Towards three dimensional aspects of plasticity-induced crack closure: A finite element simulation. *International Journal of Fatigue*, 2022, 163: 107092.

[21] G L G Gonzales, J A O. González, F V Antunes, et al. Experimental determination of the reversed plastic zone size around fatigue crack using digital image correlation. *Theoretical and Applied Fracture Mechanics*, 2023, 125: 103901.

[22] D L Chen, B Weiss, R Stickler. A model for crack closure. *Engineering Fracture Mechanics*, 1996, 53(4): 493-509.

[23] I Field, B Dixon, E Kandare, et al. The relationship between surface roughness and fatigue crack growth rate in AA7050-T7451 subjected to periodic underloads. *International Journal of Fatigue*, 2023, 167: 107355.

[24] O Gonzalez, J A P Castro, J T Meggiolaro, et al. Challenging the "ΔK_{eff} is the driving force for fatigue crack growth" hypothesis. *International Journal of Fatigue*. 2020, 136: 105577.

[25] R Pippan, G Strobl, H Kreuzer, et al. Asymmetric crack wake plasticity-a reason for roughness induced crack closure. *Acta materialia*, 2004, 52(15): 4493-4502.

[26] J Crapps, S R Daniewicz. A macrostructural model for simulating the combined effects of roughness and plasticity induced fatigue crack closure. *International Journal of Fatigue*, 2012, 45: 15-30.

[27] J Pokluda, R Pippan. Analysis of roughness-induced crack closure based on asymmetric crack-wake plasticity and size ratio effect. *Materials Science and Engineering: A*, 2007, 462(1-2): 355-358.

[28] J Pokluda, P Šandera, J Horníková. Statistical approach to roughness-induced shielding effects. *Fatigue & Fracture of Engineering Materials & Structures*, 2004, 27(2): 141-157.

[29] H A Richard, K Benitz. A loading device for the creation of mixed mode in fracture mechanics. *International Journal of Fracture*, 1983, 22: R55-R58.

[30] K H Khor, N Kamp, K D Singh, et al. Micro-mechanistic crack closure modelling of constant amplitude and variable amplitude fatigue in damage tolerant airframe aluminium alloys. *Materials Forum*. 2004, 28: 850-855.

[31] N Kamp, M R Parry, K D Singh, et al. Analytical and finite element modelling of roughness induced crack closure. *Acta Materialia*, 2004, 52(2): 343-353.

[32] M R Parry, S Syngellakis, I Sinclair. Numerical modelling of combined roughness and plasticity induced crack closure effects in fatigue. *Materials Science and Engineering: A*, 2000, 291(1-2): 224-234.

[33] K D Singh, K H Khor, I Sinclair. Roughness- and plasticity-induced fatigue crack closure under single overloads: Analytical modelling. *Acta Materialia*, 2006, 54(17): 4393-4403.

[34] Q Wang, X Liu, W Wang, et al. Mixed mode fatigue crack growth behaviour of Ni-Cr-Mo-V high strength steel weldments. *International Journal of Fatigue*, 2017, 102: 79-91.

[35] S Wang, B Yang, J Li, et al. Mixed mode crack growth behaviour considering plasticity-induced and roughness-induced closure. *Engineering Fracture Mechanics*, 2023, 289: 109430.

[36] C J Christopher, G Laboviciute, M N James, et al. Extension of the CJP model to mixed mode I and mode II. *Frattura ed Integrita Strutturale*, 2013, 7(25): 161-166.

[37] J Pokluda. Dislocation-based model of crack-tip shielding effects. *Proceedings of 1st IJFatigue and FFEMS joint workshop on characterisation of crack tip stresses, Gruppo Italiano Frattura*. Forni di Sopra, Italy, Marh 7–9, 2011: 162–169.

[38] Y Lu, F Yang, T Chen. Effect of single overload on fatigue crack growth in QSTE340TM steel and retardation model modification. *Engineering Fracture Mechanics*, 2019, 212: 81-94.

[39] E M Rodrigues, A Matias, L B Godefroid, et al. Fatigue crack growth resistance and crack closure behaviour in two aluminium alloys for aeronautical applications. *Materials Research*, 2005, 8: 287-291.

[40] Y G Xu, P J Gregson, I Sinclair. Systematic assessment and validation of compliance-based crack closure measurements in fatigue. *Materials Science and Engineering: A*, 2000, 284(1-2): 114-125.

[41] J Pokluda, P Šandera. Micromechanisms of fracture and fatigue, Springer London: Springer Science & Business Media, 2010, 125-241.

[42] X Li, J Zhang, B Yang, et al. Effect of micro-shot peening, conventional shot peening and their combination on fatigue property of EA4T axle steel. *Journal of Materials Processing Technology*, 2020, 275: 116320.

[43] L Sun, X C Zhang, R Z Wang, et al. Evaluation of fatigue and creep-fatigue damage levels on the basis of engineering damage mechanics approach. International Journal of Fatigue, 2023, 166: 107277.

[44] P G Nittur, A M Karlsson, L A Carlsson. Implementation of a plastically dissipated energy criterion for three dimensional modeling of fatigue crack growth. *International Journal of Fatigue*, 2013, 54: 47-55.

[45] F V Antunes, A G Chegini, R Branco, et al. A numerical study of plasticity induced crack closure under plane strain conditions. *International Journal of Fatigue*, 2015, 71: 75-86.

[46] K Benitz, H A Richard. Eine Bruchmechanikprobe und Belastungsvorrichtung zur Bestimmung von Rißzähigkeiten bei überlagerter Normal- und Schubbeanspruchung. *Materialwissenschaft und Werkstofftechnik*, 1981, 12(8): 297-300.

[47] H J Hoh, Z M Xiao, J Luo. On the plastic zone size and crack tip opening displacement of a Dugdale crack interacting with a circular inclusion. *Acta Mechanica*, 2010, 210(3): 305-314.

[48] Y M Zhang, Z M Xiao, W G Zhang. On 3-D crack problems in offshore pipeline with large plastic deformation. *Theoretical and Applied Fracture Mechanics*, 2013, 67: 22-28.

[49] L Achchhe, M B Vaghela. Numerical investigation of an orthotropic plate with interactions of crack, inclusions and oids under uniaxial tensile loading by XFEM. *International Journal of Applied Mechanics*, 2020, 12(10): 2050113.

[50] F Erdogan, G C Sih. Closure to "Discussion of 'On the crack extension in plates under plane loading and transverse shear'". *Journal of Basic Engineering*, 1963, 85(4): 519-525.

[51] G C Sih, B MacDonald. Fracture mechanics applied to engineering problems-strain energy density fracture criterion. *Engineering Fracture Mechanics*, 1974, 6(2): 361-386.

[52] P Zhang, L Xie, C Zhou, et al. Experimental and numerical investigation on fatigue cack growth behavior of commercial pure titanium under I-II mode loading at negative load ratios. *International Journal of Fatigue*, 2020, 138: 105700.

[53] S Suresh, R O Ritchie. A geometric model for fatigue crack closure induced by fracture surface roughness. *Metallurgical transactions A*, 1982, 13: 1627-1631.

[54] M N James, M N Pacey, L W Wei, et al. Characterisation of plasticity-induced closure-crack flank contact force versus plastic enclave. *Engineering Fracture Mechanics*, 2003, 70(17): 2473-2487.

Shuancheng Wang born in 1994, is currently a PhD candidate at the *State Key Laboratory of Rail Transit Vehicle System, Southwest Jiaotong University, China*. His research interests include fatigue analysis and structural reliability.

Bing Yang born in 1979, is currently a professor at the *State Key Laboratory of Rail Transit Vehicle System, Southwest Jiaotong University, China*. He received his PhD degree from *Southwest Jiaotong University, China*, in 2011. His research interests include strength of vehicle structure and fatigue and fracture of materials.

Shuwei Zhou born in 1998, is currently a PhD candidate at the *Institute of Metal Forming, RWTH Aachen University, Germany*. His research interests include structural micromechanics and machine learning.

Jian Li born in 1998, is currently a master candidate at the *State Key Laboratory of Rail Transit Vehicle System, Southwest Jiaotong University, China*. His research interests include fracture mechanics and damage tolerance analysis.

Shoune Xiao born in 1964, is currently a professor at *State Key Laboratory of Traction Power, Southwest Jiaotong University, China*. He received his master's degree from *Southwest Jiaotong University, China*, in 1988. His research interests include vehicle dynamics, collision, structural strength and fatigue reliability.